nature chemical biology

ARTICLES

https://doi.org/10.1038/s41589-019-0268-8

Dynamic assembly of protein disulfide isomerase in catalysis of oxidative folding

Masaki Okumura[1,2,9*], Kentaro Noi[3,4,5,9], Shingo Kanemura[1,2], Misaki Kinoshita[2], Tomohide Saio[6], Yuichi Inoue[1], Takaaki Hikima[7], Shuji Akiyama[7,8], Teru Ogura[3,5*] and Kenji Inaba[1,5*]

Time-resolved direct observations of proteins in action provide essential mechanistic insights into biological processes. Here, we present mechanisms of action of protein disulfide isomerase (PDI)—the most versatile disulfide-introducing enzyme in the endoplasmic reticulum—during the catalysis of oxidative protein folding. Single-molecule analysis by high-speed atomic force microscopy revealed that oxidized PDI is in rapid equilibrium between open and closed conformations, whereas reduced PDI is maintained in the closed state. In the presence of unfolded substrates, oxidized PDI, but not reduced PDI, assembles to form a face-to-face dimer, creating a central hydrophobic cavity with multiple redox-active sites, where substrates are likely accommodated to undergo accelerated oxidative folding. Such PDI dimers are diverse in shape and have different lifetimes depending on substrates. To effectively guide proper oxidative protein folding, PDI regulates conformational dynamics and oligomeric states in accordance with its own redox state and the configurations or folding states of substrates.

Cells have elaborate systems to promote protein folding[1]. A representative example is the disulfide bond formation network of the mammalian endoplasmic reticulum (ER)[2,3]. The ER folds approximately 30% of all proteins produced by the cell[4], the majority of which require disulfide bonds during maturation. Whereas structural disulfides stabilize local or global conformations of folding intermediates and native-state proteins by decreasing the configurational entropy of unfolded states[5–7], non-native disulfides cause aberrant structures and sometimes aggregation of proteins, resulting in the pathogenesis of misfolding diseases[8–10]. Protein homeostasis in the ER is guaranteed by the disulfide bond formation network, which consists of more than 20 kinds of protein disulfide isomerases (PDIs) and several upstream PDI oxidases[11,12], of which the canonical PDI is the most versatile catalyst of disulfide bond formation[13–15]. PDI selectively and effectively introduces native disulfide bonds into various substrates, ensuring both efficiency and fidelity of oxidative protein folding[16,17]. The ER-resident flavoenzyme endoplasmic reticulum oxidoreductin-1α (Ero1α) donates its oxidative power preferentially to PDI[18–21], implying that PDI serves as a primary catalyst in oxidative protein folding in the ER.

PDI contains four thioredoxin-like domains arranged in the order **a**, **b**, **b′** and **a′** from the N-terminus and adopts a U-shaped domain arrangement in which the redox-active Cys–Gly–His–Cys motifs of domains **a** and **a′** face each other across the central cleft[22]. The cleft inside the U contains a hydrophobic surface, enabling the enzyme to specifically bind unfolded or misfolded substrates[23–26]. These structural and mechanistic features are likely shared by the homologs of canonical PDI from yeast to human[24,27].

Redox-dependent domain rearrangement is commonly observed with PDI from multiple species[27,28]. Crystal structures of human PDI show that the reduced form has a more closed domain arrangement than the oxidized form. Consequently, the volume of the central cleft in the reduced form (~6,800 Å^3) is less than half of that in the oxidized form (~14,400 Å^3)[27]. In this context, redox-dependent binding and release by PDI has been reported for several substrates, including cholera toxin[29], the α-subunit of prolyl-4-hydroxylase[30] and antigen peptides[31], suggesting that the redox state is key to regulating the specificity and affinity for substrates of PDI.

Despite the accumulating number of structural and mechanistic insights into PDI[32], the actual mechanism of action of this enzyme has not been fully elucidated; one of the primary reasons could be that no direct observation has been made for its catalysis of oxidative protein folding. Here we sought to visualize the dynamic actions of PDI in the presence or absence of substrates, at the single-molecule level, by high-speed atomic force microscopy (HS-AFM)[33–35]. Strikingly, unfolded substrates induced PDI to form a face-to-face dimer, creating a central hydrophobic cavity designed to accommodate substrates. Our findings shed light on the physiological significance of substrate-induced PDI dimerization and suggest a new model for the mechanism of PDI in effectively guiding oxidative protein folding.

Results

A redox-dependent conformational switch of PDI. Crystal structures of human PDI in reduced and oxidized states show that reduced PDI assumes a closed U-shape with a twisted configuration, whereas oxidized PDI adopts a more open and flat domain arrangement[27]. To analyze redox-dependent conformational changes of human PDI in solution, we carried out small-angle X-ray scattering (SAXS) measurements. The values for radius of gyration, R_g, were estimated to be 35.8 ± 0.2 Å and 37.2 ± 0.2 Å for the reduced and oxidized forms, respectively (Supplementary Table 1). The molecular mass, calculated from the normalized forward intensity value using bovine

[1]Institute of Multidisciplinary Research for Advanced Materials, Tohoku University, Sendai, Japan. [2]Frontier Research Institute for Interdisciplinary Sciences, Tohoku University, Sendai, Japan. [3]Institute of Molecular Embryology and Genetics, Kumamoto University, Kumamoto, Japan. [4]Graduate School of Engineering, Osaka University, Suita, Japan. [5]CREST, JST, Tokyo, Japan. [6]Department of Chemistry, Faculty of Science, Hokkaido University, Sapporo, Japan. [7]RIKEN SPring-8 Center, RIKEN Harima Institute, Sayo-cho, Japan. [8]Research Center of Integrative Molecular System (CIMoS), Institute for Molecular Science, National Institute of Natural Sciences, Okazaki, Japan. [9]These authors contributed equally: Masaki Okumura, Kentaro Noi.
*e-mail: okmasaki@mail.tagen.tohoku.ac.jp; ogura@gpo.kumamoto-u.ac.jp; kinaba@tagen.tohoku.ac.jp

serum albumin as a standard, was 56.3 kDa for the reduced form and 55.7 kDa for the oxidized form. Thus, although both forms are monomeric, the oxidized form assumes a more extended conformation than the reduced form (Supplementary Fig. 1a, b and Table 1), consistent with crystallographic observations. However, the SAXS profiles of reduced and oxidized PDI disagreed significantly with those calculated from their crystal structures (Supplementary Fig. 1c), indicating that PDI adopts different conformations in solution.

To directly visualize redox-dependent conformational changes in PDI at the single-molecule level, we employed HS-AFM[33–36] (Fig. 1). For these experiments, the N-terminal His-tag segment was immobilized onto a Co^{2+}-conjugated mica surface. When the N-terminal His_6-tag was cleaved off, the number of PDI molecules bound to the surface decreased by approximately 80% (Supplementary Fig. 2a), suggesting that the immobilization of PDI to the mica surface is mediated primarily through the interaction between the His_6-tag and Co^{2+} scattered on the surface. Under this experimental setting, approximately 15 PDI molecules were observed in the observation area of 5,000 × 5,000 Å^2, excluding the possibility of artefactual protein–protein contacts on the mica surface. Successive AFM images acquired every 100 ms revealed that, in the presence of 2 μM reduced glutathione (GSH)/1 μM oxidized glutathione (GSSG), PDI molecules underwent dynamic domain rearrangement (Supplementary Fig. 2b). By contrast, after pretreatment with the reducing reagent DTT, all PDI molecules adopted much less dynamic and more compact conformations (Fig. 1a). Such redox-dependent conformational regulation was also observed with His-tag-deleted PDI (ΔHis-PDI) (Supplementary Fig. 2c), suggesting that the interactions between PDI and the mica surface are weak enough for PDI to maintain its intrinsic structural nature.

For reduced PDI, the histograms of the long- and short-axis lengths and heights calculated based on hundreds of molecules were nicely fitted by a single-Gaussian distribution with peak lengths of 86 ± 12 Å, 76 ± 10 Å and 23 ± 6 Å, respectively (Fig. 1c, top). The two-dimensional scatterplot of the long versus short axes emphasizes the single conformational population. To validate the number of states assumed in data fitting, we further calculated the Akaike's information criterion (AIC) scores by analyzing the two particle dimensions along the long and short axes together (Fig. 1c, top) or the three particle dimensions (long- and short-axis lengths and height) separately (Supplementary Fig. 3a; for more details, see Methods). The AIC analyses indicated that a single-state model best explains the conformational population of reduced PDI. Consistently, the long-axis length remained constant at around 90 Å (Fig. 1d, top; see also Supplementary Video 1), indicating that reduced PDI maintains the closed conformation throughout the measurement period.

By contrast, PDI molecules pretreated with the oxidizing reagent diamide existed as two populations: one 82 ± 9 Å long and 22 ± 5 Å high, and the other 111 ± 17 Å long and 13 ± 2 Å high (Fig. 1c, bottom). In support of this, the histograms of oxidized PDI for the long-axis length and height were better fitted by a two-Gaussian distribution than by a single-Gaussian distribution (Fig. 1c, bottom, and Supplementary Fig. 3a). The two-dimensional scatterplot of the long- versus short-axis lengths more clearly indicates the existence of one major (closed) and one minor (open) conformations for oxidized PDI (Fig. 1c, bottom). Thus, the fractions of the former and latter forms were estimated to be 68.5% and 31.5%, respectively. The AIC analysis corroborates two conformational populations of oxidized PDI (Fig. 1c, bottom, and Supplementary Fig. 3a).

The HS-AFM analysis further demonstrated that the long-axis length of oxidized PDI varied in the range 80–140 Å in a reversible manner (Fig. 1d, bottom, Supplementary Fig. 4a,b and Supplementary Video 2). The histogram calculated on the basis of this time trace was similar to that based on AFM images of hundreds of molecules. Thus, the oxidized enzyme is in dynamic equilibrium between the open/flat and twisted/closed conformations.

In the crystal structure, reduced PDI adopts a closed/twisted conformation stabilized by the cation–π interaction between Arg300 and Trp396 (Supplementary Fig. 5a,b)[27]. This interaction is disrupted on formation of the Cys397–Cys400 disulfide, preventing oxidized PDI from maintaining the closed/twisted conformation. Accordingly, the Arg300Ala mutant exhibited two alternating conformations with different long-axis lengths, even in the reduced form, as revealed by the HS-AFM analysis (Fig. 2a,b, Supplementary Fig. 3b, left, and Supplementary Fig. 4c). However, the mutant displayed a single population peak at a length of approximately 16 Å for the height unlike the oxidized form of wild-type PDI (Figs. 1c and 2a and Supplementary Fig. 3b, left), suggesting that the mutant could no longer maintain a closed/twisted conformation. Notably, the mutant had lower RNase A refolding activity than the wild-type protein (Fig. 2c), although both proteins were oxidized by human Ero1α at similar rates (Fig. 2d) and had a similar affinity (15–19 μM) and stoichiometry (approximately 1:1) for mastoparan, a 14-residue model substrate that contains no disulfide bonds but binds to the substrate-binding pocket in the PDI **b′** domain[23] (Fig. 2e and Supplementary Fig. 6). Because reduced PDI primarily engages in isomerization of non-native disulfide bonds formed in folding intermediates, the closed conformation of reduced PDI is more likely suited to recognize and trap relatively compact and structured species. Thus, redox-regulated conformational dynamics are critical for PDI to achieve its maximal activity in catalyzing oxidative protein folding.

Fig. 1 | Redox-dependent regulation of PDI dynamics. a, Schematic structures and AFM images (scan area, 150 × 150 Å^2; scale bar, 50 Å) of reduced (top) and oxidized (bottom) forms of PDI (see also Supplementary Videos 1 and 2 for reduced PDI and oxidized PDI, respectively). The experiments were independently repeated 67 times for reduced PDI and 62 times for oxidized PDI, and the same trends were seen in all of the experiments. **b**, Cartoon of spatial domain arrangement of PDI. The four thioredoxin domains, arranged in the order **a**, **b**, **b′** and **a′** from the N-terminus, and the C-terminal α-helical domain **c** are depicted by boxes. Active-site sequences (CGHC) are shown in the boxes of the **a** and **a′** domains. **c**, Two-dimensional scatterplots of the long- versus short-axis lengths for reduced (top) and oxidized (bottom) PDI molecules observed by HS-AFM. A red dot corresponds to each observed molecule (n = 582 for oxidized PDI and n = 484 for reduced PDI), and the occurrence frequency is represented as a gray scale. One-dimensional histograms with Gaussian fitting curves for long- and short-axis lengths are shown on the top and right sides of the two-dimensional plots, respectively. One-dimensional histograms for heights of reduced (top) and oxidized (bottom) forms of PDI are shown on the top-right side of the plots. Average length values (mean ± s.d.) are shown for each axis. The AIC scores calculated by analyzing the two particle dimensions along the long and short axes together with multiple-state (one to four) models are shown on the bottom-right side of the plots. To highlight the redox-dependent conformational changes of monomeric PDI species, a minor fraction (~10%) of PDI dimers were excluded from calculation of the histograms. All data were analyzed using the IGOR Pro 6.0 software. **d**, Left: time trace of the long-axis length for reduced (top) and oxidized (bottom) forms of PDI. Right: histograms of the long-axis length calculated from the time traces shown in the left panels (630 and 401 time points for oxidized and reduced forms of PDI, respectively). Values represent the average long-axis length (mean ± s.d.) calculated from the curve fitting with a single- (reduced PDI) or two- (oxidized PDI) Gaussian model. The experiments were repeated for five independent particles of reduced PDI and six independent particles of oxidized PDI, and the same trends were seen for all particles.

Unfolded substrates induce PDI dimerization. To determine whether substrate binding affects the conformational dynamics of PDI, we performed HS-AFM measurements for oxidized PDI in the presence of mastoparan. On addition of the peptide, the long-axis length of PDI decreased to 72 ± 10 Å for the closed form and 96 ± 11 Å for the open form, and the ratio of the closed form relative to the open form increased significantly (60.1% versus 39.9%) (Fig. 2f). Moreover, the amplitude of fluctuation in the long-axis direction decreased (Fig. 2g and Supplementary Fig. 4d). These results indicate that substrate binding rendered oxidized PDI more compact and less dynamic.

Next, we employed bovine pancreas trypsin inhibitor (BPTI), with a molecular weight of ~6,500 and three structural disulfide bonds, as a model protein substrate. To prepare constitutively reduced and unfolded BPTI, all of its cysteine residues were blocked with maleimide-ATTO532 (Cys-blocked BPTI; Supplementary Fig. 7a). HS-AFM analyses revealed that a significant fraction of oxidized PDI formed a face-to-face homodimer on addition of Cys-blocked BPTI (Fig. 3a), and that the dimer persisted stably throughout the observation time window of over 20 s (Supplementary Figs. 7b and 13c). It is unlikely that the PDI dimerization was caused by the close proximity of PDI molecules on the mica plate, because most (~90%) of the PDI molecules were observed separately as monomers in the absence of Cys-blocked BPTI (Fig. 3b). Indeed, under this observation condition, not all PDI molecules were immobilized and some likely diffused in solution on the mica plate.

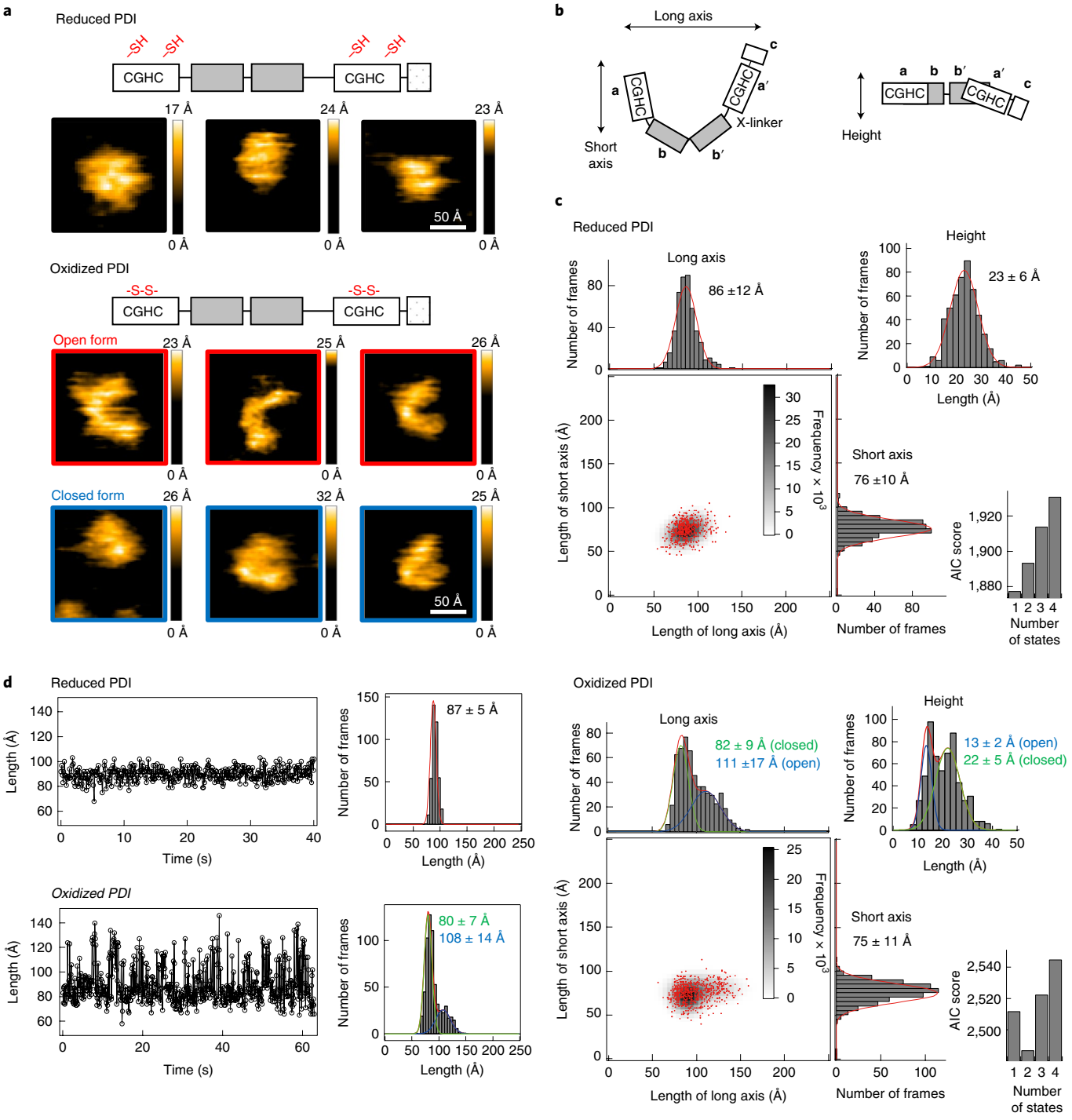

The abundance of the dimer species increased with the concentration of Cys-blocked BPTI: its occupancy reached approximately 60% when Cys-blocked BPTI was present in 30-fold molar excess relative to PDI (Fig. 3b). Similar results were obtained using another BPTI derivative, NEM-blocked BPTI, in which all Cys residues were modified with *N*-ethylmaleimide (NEM) instead of maleimide-ATTO532 (Supplementary Fig. 8a). This observation suggests that the bulkiness and hydrophobicity of Cys-blocking reagents barely affect the substrate-induced dimerization of PDI.

To verify that substrate-induced PDI dimerization takes place in solution as well as on mica plates, we analyzed the oligomeric state of oxidized PDI by size-exclusion chromatography combined with multi-angle light scattering (SEC-MALS) at various molar ratios of NEM-blocked BPTI to oxidized PDI (Supplementary Fig. 9a,b). In the absence of substrate, the ratio of dimer to monomer was almost constant at around 0.15, regardless of the PDI concentration (Supplementary Fig. 9a). By contrast, NEM-blocked BPTI increased the proportion of PDI dimer to 34.7% (Supplementary Fig. 9b), supporting our finding that unfolded BPTI induces PDI dimerization in solution.

To directly visualize the substrate bound to PDI, reduced and unfolded BPTI conjugated to an Au particle with a diameter of approximately 2 nm via free cysteines (Au-conjugated BPTI) was added to oxidized PDI. HS-AFM analysis demonstrated that Au-conjugated BPTI bound to the central cleft of monomeric PDI (Supplementary Fig. 7c, left), confirming that this site actually serves as a substrate-binding space of the enzyme. It is also noted that some Au-conjugated BPTI bound to the central cavity created by a face-to-face dimer of oxidized PDI (Supplementary Fig. 7c, right), suggesting that this cavity serves to accommodate an unfolded substrate.

In contrast to the oxidized form of PDI, a redox-inactive PDI mutant (PDI AxxA-AxxA), in which the active-site cysteines in the **a** and **a′** domains are both mutated to alanine to mimic the reduced form, formed only a minor fraction of homodimer in the presence of excess Cys-blocked BPTI (Supplementary Fig. 8b). Thus, dimerization induced by unfolded substrate was observed exclusively with oxidized PDI, suggesting a link between redox-dependent conformational dynamics and PDI dimerization.

Repeated assembly of PDI in oxidative protein folding. To further explore the actions of PDI in the catalysis of oxidative protein folding, we added reduced and denatured BPTI without a cysteine block, that is, foldable BPTI, to oxidized PDI. Under these conditions, PDI repeatedly associated into dimers and dissociated into monomers with a period of approximately 1 s (Fig. 3c,d and Supplementary Video 3). This observation suggests that a non-immobilized PDI molecule binds to and subsequently dissociates from another immobilized PDI monomer, depending on the folded states of the substrate. Thus, foldable BPTI-induced PDI dimerization only occurred transiently (Fig. 3c,d), whereas constitutively unfolded (Cys-blocked) BPTI generated stable PDI dimers (Supplementary Fig. 7b). We infer that oxidized PDI binds reduced/denatured BPTI to form a homodimer, which disassembles into monomers after thiol-disulfide exchanges between PDI and BPTI and subsequent release of disulfide-bonded BPTI. Thus, PDI likely undergoes striking intramolecular and intermolecular dynamics in accordance with its own redox state and the folding states of its substrates.

PDI dimerization depends on folding states of substrates. Since PDI is supposed to act on partially structured folding intermediates[15] as well as on unfolded substrates[37], we next investigated whether folding intermediates can also influence the dimeric state of PDI. To this end, we prepared BPTI des[51–30] (N*) as a model folding intermediate by selectively modifying the Cys30 and Cys51 residues with NEM (Supplementary Fig. 10a–c), and added it to oxidized PDI. Statistical analysis of HS-AFM images showed that in the presence of a large excess of reduced/unfolded, intermediate or native BPTI, the fraction of oxidized PDI dimer was 58.3%, 26.6% or 12.0%, respectively (Fig. 3e). Thus, folding intermediates are less able to induce PDI dimerization than unfolded substrates. In contrast to that of oxidized PDI, the dimer-to-monomer ratio of reduced PDI was insensitive to reduced/unfolded, intermediate and native BPTI (Fig. 3e). In line with this, PDI AxxA-AxxA did not appreciably increase the dimer fraction in the presence of an excess of reduced/unfolded BPTI (Supplementary Fig. 8b), again indicating the link between the redox-dependent conformational dynamics and substrate-induced dimerization of PDI.

Conformational diversity of PDI dimers. Given that oxidized PDI forms dimers to promote initial introduction of disulfide bonds into highly flexible unfolded substrates, we surmised that this dimeric state also undergoes significant conformational dynamics.

Fig. 2 | Significance of redox-dependent regulation of PDI dynamics in catalysis of oxidative protein folding. a, Two-dimensional scatterplots of the long- versus short-axis lengths for reduced PDI Arg300Ala mutant molecules observed by HS-AFM. A red dot corresponds to each observed molecule ($n = 308$), and the occurrence frequency is represented as a gray scale. One-dimensional histograms with Gaussian fitting curves for long- and short-axis lengths are shown on the top and right sides of the two-dimensional plot, respectively. Average length values (mean ± s.d.) are shown for each axis. A one-dimensional histogram for height (top right) and calculated AIC scores using multiple-state (one to four) models (bottom right) are also shown. **b**, Left: time course of the long-axis length of reduced PDI Arg300Ala mutant. Right: histogram of the long-axis length calculated from the time trace (382 time points) shown in the left panel. Values represent the average long-axis length (mean ± s.d.) calculated from the curve fitting with a two-Gaussian model. The experiment was repeated for five independent particles of PDI Arg300Ala, and the same trend was seen for all particles. **c**, RNase A refolding activity of PDI wild type and Arg300Ala in the presence of human Ero1α. Reduced and denatured RNase A (25 μM) was incubated at 30 °C with 2 μM human Ero1α and 10 μM PDI wild type or Arg300Ala mutant in 50 mM Tris-HCl (pH 7.5) containing 300 mM NaCl. Buffer was air-saturated. The time course of recovery of RNase A activity was measured by the decay in absorbance at 295 nm, using cytidine 2′,3′-cyclic monophosphate monosodium salt as a substrate of RNase A. Values represent means ± s.d. of three independent experiments. **d**, Oxidation of PDI wild type and Arg300Ala mutant (10 μM) by human Ero1α (2 μM) was monitored by measuring the decrease in absorbance at 340 nm, which is ascribed to NADPH (200 μM) consumption catalyzed by glutathione reductase in buffer containing GSH (1 mM) and PDI wild type or Arg300Ala mutant (10 μM). The experiment was independently repeated three times with reproducible results. **e**, Binding of mastoparan to the reduced form of PDI wild type/PDI R300A was monitored by ITC. See also raw data shown in Supplementary Fig. 6. Bars represent the means ± s.e.m of three independent experiments analyzed by Origin software. **f**, Two-dimensional scatterplots of the long- versus short-axis lengths for oxidized PDI molecules ($n = 200$) in the presence of mastoparan (130 nM) observed by HS-AFM. One-dimensional histograms with Gaussian fitting curves for long- and short-axis lengths are displayed on the top and right sides of the two-dimensional plot, respectively. Average length values (mean ± s.d.) are shown for each axis. A one-dimensional histogram for height (top right) and calculated AIC scores using multiple-state (one to four) models (bottom right) are also shown. **g**, Top: time trace of the long-axis length of mastoparan-bound PDI. Bottom: histogram of the long-axis length calculated from the time trace (382 time points) shown in the top panel. Values represent the average long-axis length (mean ± s.d.) calculated from the curve fitting with a two-Gaussian model. The experiment was repeated for five independent particles of mastoparan-bound PDI, and the same trend was seen for all particles.

To explore this possibility, we statistically analyzed HS-AFM images of PDI dimers formed in the presence of reduced/unfolded (Cys-blocked) or intermediate (NEM-modified) BPTI. Of interest, PDI dimers induced by Cys-blocked BPTI assume multiple conformations. The two-dimensional scatterplot of the long- versus short-axis lengths and the AIC analysis clearly shows two conformational populations of PDI dimers (Fig. 4a and Supplementary Fig. 3c). Thus, we found that PDI dimers exist as loosely and tightly associated forms with a long-axis length of 135 ± 18 and 95 ± 11 Å, respectively (Fig. 4a). By contrast, the conformational population of intermediate BPTI-induced PDI dimers was best fitted by a single-state model consisting of a single conformation with a long-axis length of 116 ± 20 Å (Fig. 4b and Supplementary Fig. 3c). Although it is hard to precisely define the structure, and hence the mode of assembly, of each PDI dimer due to the resolution limit of HS-AFM, loosely associated dimers appear heterogenous in shape, with some consisting of a central cavity with a gaping exit (Fig. 4c). Such structural diversity of PDI dimers suggests that interactions between two PDI molecules are weak and transient, and vary depending on the multiple configurations of unfolded substrates. Thus, oxidized PDI has

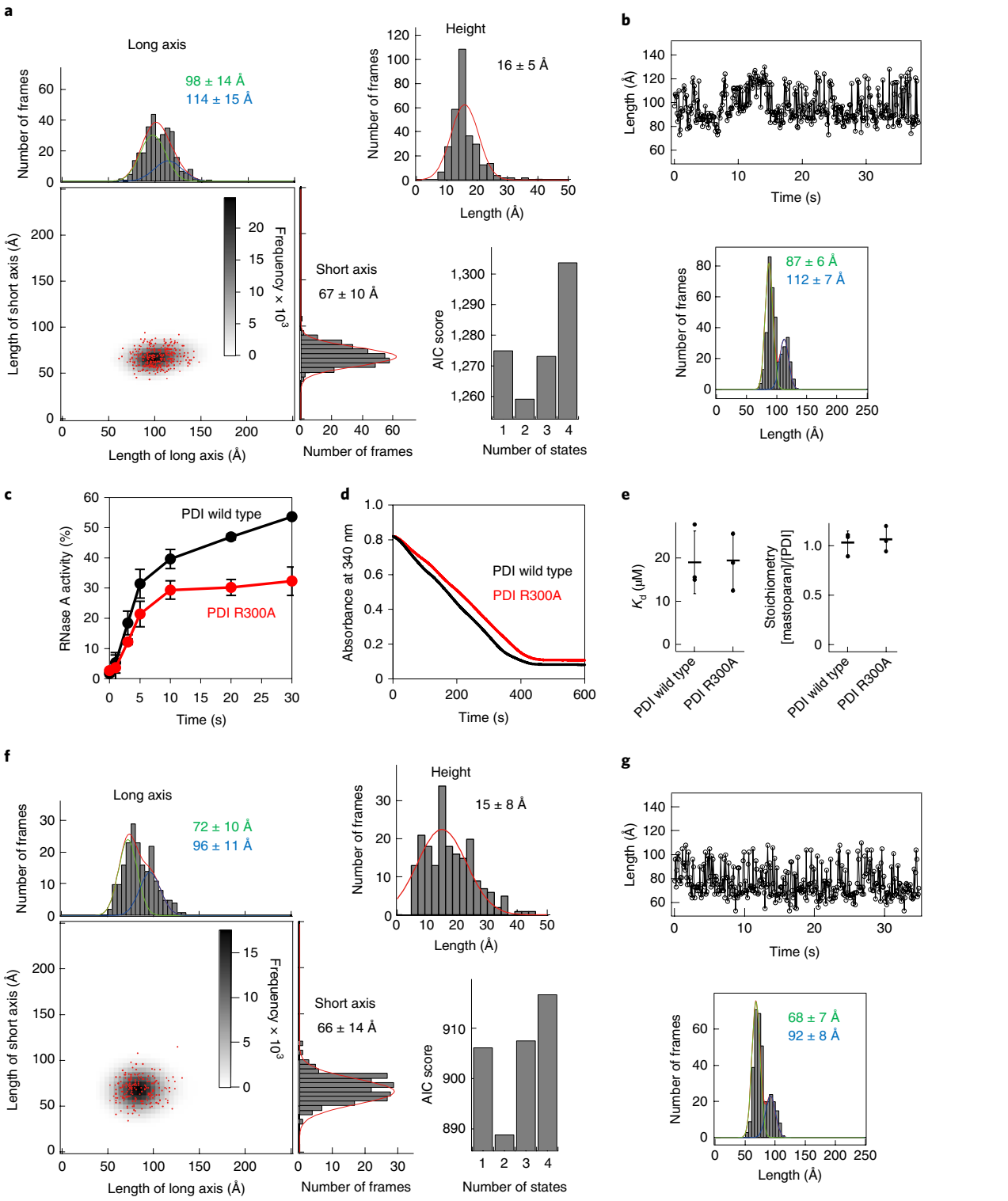

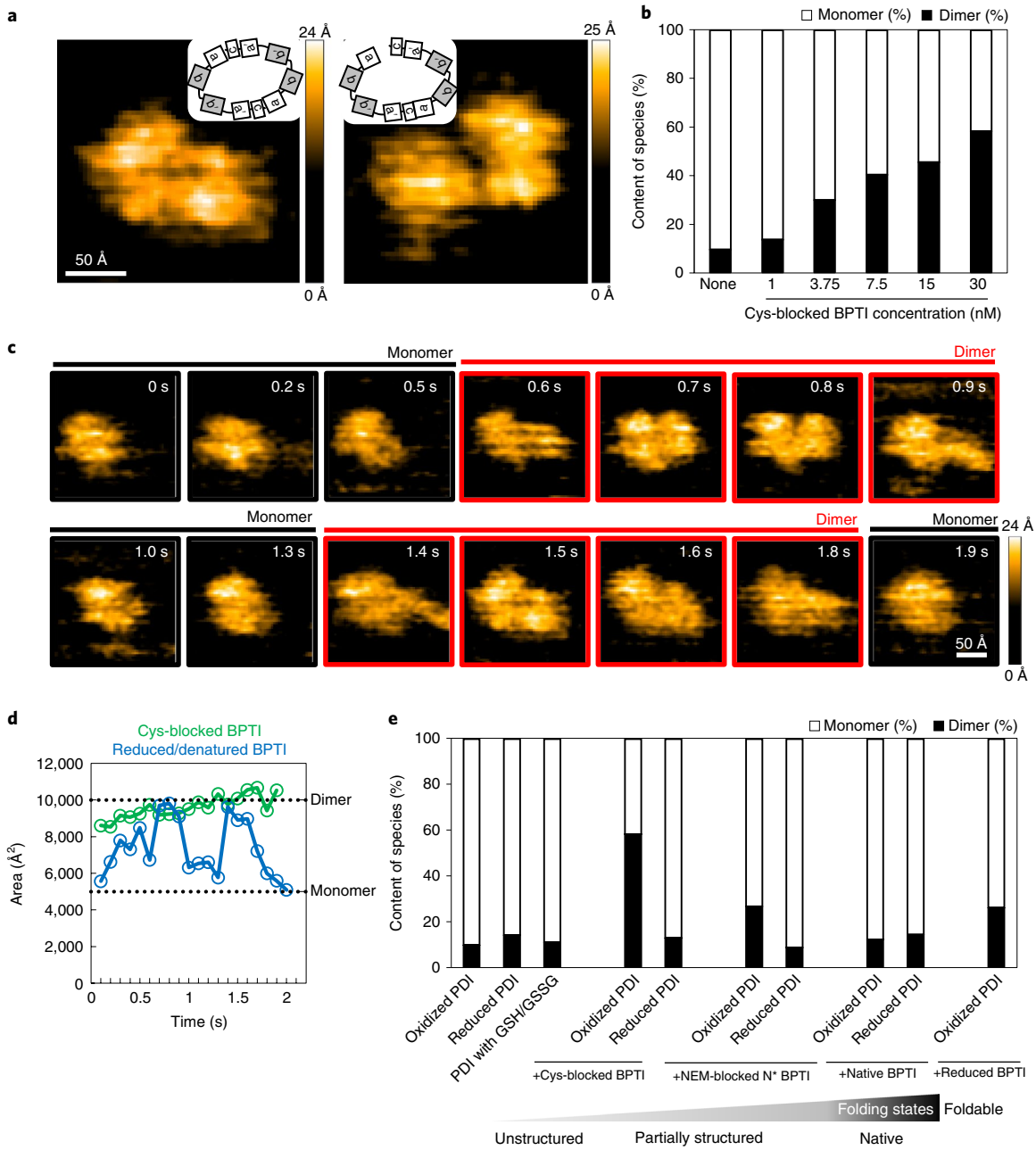

Fig. 3 | Unfolded substrate-induced dimerization of oxidized PDI. a, Typical AFM images of the oxidized form of PDI (1 nM) in the presence of 30 nM Cys-blocked BPTI (scan area, 200 × 200 Å^2; scale bar, 50 Å) and simplified cartoons of observed PDI dimers. The experiment was independently repeated 32 times, and the same trend was seen in all of the experiments. **b**, Dimer-to-monomer ratio of oxidized PDI in the presence of different concentrations of Cys-blocked BPTI (n = 335, 279, 307, 292, 309 and 290 independent particles for 0, 1, 3.75, 7.5, 15 and 30 nM Cys-blocked BPTI, respectively), analyzed by HS-AFM. **c**, Successive AFM images of oxidized form of PDI (1 nM) in the presence of 30 nM reduced and denatured BPTI (see also Supplementary Video 3). The experiment was independently repeated 61 times, and the same trend was seen in all of the experiments. **d**, Time course of the area of the observed PDI molecule in the HS-AFM snapshots shown in **c** and Supplementary Fig. 7b. **e**, PDI dimerization in the presence of substrates of different folding states. Ratios of dimer (black box) to monomer (white box) were calculated based on the HS-AFM images of oxidized PDI alone, reduced PDI alone, PDI with 2 μM GSH and 1 μM GSSG, and mixtures of oxi/red PDI with Cys-blocked (unfolded) BPTI, NEM-modified N* (folding intermediate) BPTI, native BPTI, and reduced/denatured BPTI (n = 335, 359, 315, 290, 322, 290, 313, 326, 317 and 281 independent particles, respectively). PDI and BPTI concentrations were 1 nM and 30 nM, respectively.

high plasticity both as dimer and monomer (Fig. 1a–c and Fig. 4), likely facilitating adjustment to substrates of varying conformations along their folding pathways.

Physiological significance of PDI dimers. To explore the physiological significance of the substrate-induced dimers, we measured the rate of BPTI folding at different PDI concentrations in the presence of GSH (2 mM)/GSSG (1 mM) (Fig. 5a and Supplementary Fig. 11). From the HPLC profiles, we calculated rate constants for conversion from the unfolded state to intermediate states (k_1) and from intermediate states to native state (k_2) at each PDI concentration. k_1 increased nonlinearly with PDI concentration (Fig. 5a, left,

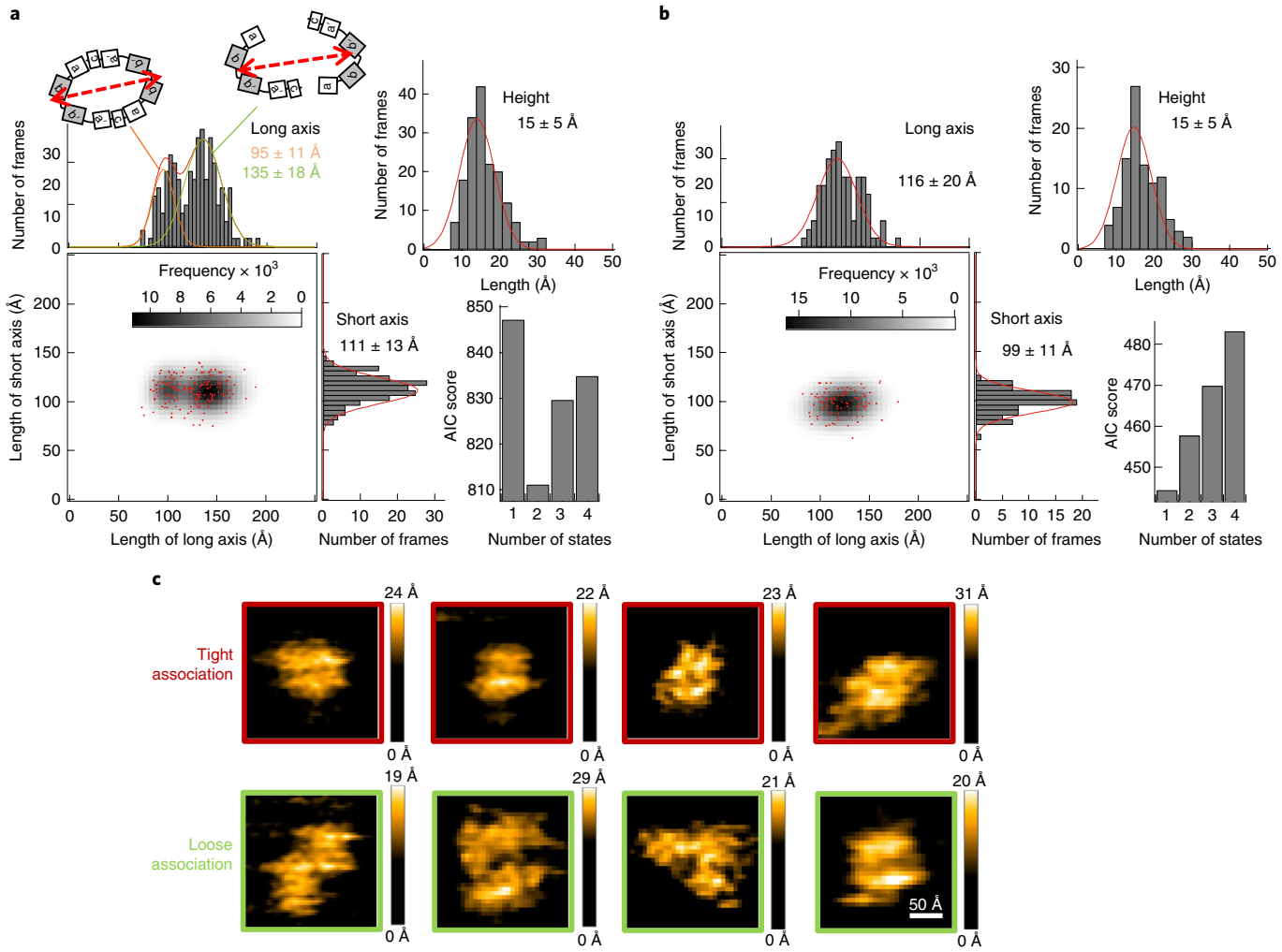

Fig. 4 | Structural diversity of substrate-induced PDI dimers. a, Two-dimensional scatterplots of the long- versus short-axis lengths for PDI dimer molecules in the presence of Cys-blocked BPTI observed by HS-AFM. A red dot corresponds to each observed molecule ($n=169$), and the occurrence frequency is represented as a gray scale. One-dimensional histograms with Gaussian fitting curves for long- and short-axis lengths are shown on the top and right sides of the two-dimensional plot, respectively. Average length values (mean ± s.d.) are shown for each axis. A one-dimensional histogram for height (top right) and calculated AIC scores using multiple-state (one to four) models (bottom right) are also shown. Values represent the average long-axis length (means ± s.d.) calculated using the IGOR Pro 6.0 software. **b**, Two-dimensional scatterplots of the long- versus short-axis lengths for PDI dimer molecules in the presence of NEM-modified N* BPTI observed by HS-AFM. A red dot corresponds to each observed molecule ($n=100$). Average length values (mean ± s.d.) are shown for each axis. A one-dimensional histogram for height (top right) and calculated AIC scores using multiple-state (one to four) models (bottom right) are also shown. **c**, Representative AFM images of tightly or loosely associated PDI dimers formed in the presence of Cys-blocked BPTI. The experiment was independently repeated 170 times, and the same trend was seen in all of the experiments.

and Supplementary Fig. 12), while k_2 increased linearly with PDI concentration, as in normal enzymatic reactions (Fig. 5a, right, and Supplementary Fig. 12). Thus, unlike late folding steps starting from intermediate states, the initial disulfide introduction step starting from the unfolded state was synergistically accelerated by elevated PDI concentration. Rate constant k_1 (32.7 min^{-1}) at a PDI concentration of 20 μM was approximately 2.5-fold higher than the value calculated by assuming that the rate constant is a linear function of PDI concentration (13.2 min^{-1}). Taking also into account that 33.4% of PDI molecules form a dimer at this concentration (20 μM) in the presence of unfolded BPTI (Fig. 5b), we estimated that the PDI dimer accelerates k_1 by approximately 7.5-fold. Thus, substrate-induced PDI dimers have the ability to greatly accelerate introduction of disulfide bonds into unfolded substrates.

Generality of substrate-induced PDI dimerization. To investigate the generality of transient PDI dimerization in the presence of foldable substrates, we employed another substrate, reduced and denatured RNase A, with a molecular weight of approximately 14,000 and four disulfide bonds. This substrate also induced PDI dimerization, but the lifetime of the RNase A-induced PDI dimer was significantly longer than that of the BPTI-induced dimer (Supplementary Fig. 13a and Supplementary Video 4). Time-resolved HS-AFM images revealed that PDI dimers underwent repeated expansion and contraction in the long-axis direction in the presence of reduced and denatured RNase A (Fig. 6a). Assuming that RNase A was accommodated in the central cavity created by the PDI dimer, these persistent and transformable PDI dimers might be ascribed to the slower and more complicated folding mechanism of RNase A than that of BPTI[15] (see also Discussion). Statistical analysis of the HS-AFM images revealed that reduced and denatured RNase A generated long-lived PDI dimers at a higher yield than reduced and denatured BPTI; nearly 37.0% of RNase A-induced PDI dimers had a lifetime longer than

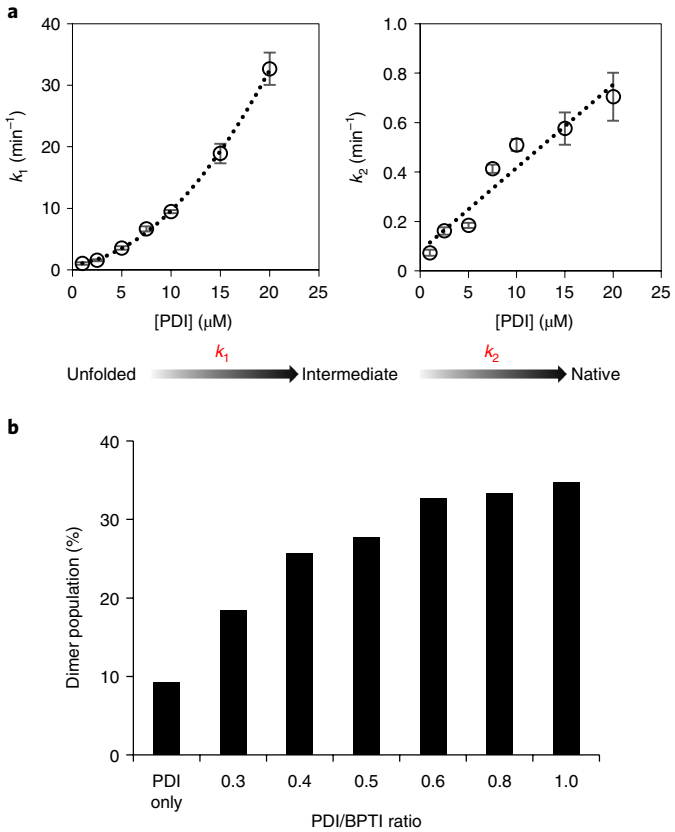

Fig. 5 | Physiological significance of PDI dimers in oxidative folding of BPTI. a, Rate constants of oxidative folding of PDI-catalyzed BPTI in the presence of GSH/GSSG (2 mM/1 mM) as a function of PDI concentration. The native, intermediate, and reduced and denatured species of BPTI were separated by HPLC and quantitated (see also raw data in Supplementary Fig. 11). Rate constants k_1 and k_2 were determined by curve fitting using IGOR Pro 6.0 software (see Supplementary Fig. 12). Values are means ± s.d. of three independent experiments. **b**, Dimer population of oxidized PDI (7.5–25 μM) in the presence of Cys-blocked BPTI (25 μM), as determined by SEC-MALS (see Supplementary Fig. 9c). The experiment was performed once at all mixing ratios.

5 s (Fig. 6b, top), versus only 6.8% when BPTI was the substrate (Fig. 6b, bottom). Consistent with this, the fractions of PDI dimers with a lifetime shorter than 0.5 s significantly decreased when RNase A was used as a substrate (Fig. 6b).

A minor fraction (~10%) of oxidized PDI molecules formed short-lived dimers even without substrates (Fig. 3b and Supplementary Fig. 13b, right panel), indicating the existence of substrate-independent PDI dimers. As expected, the addition of Cys-blocked BPTI significantly increased the population of PDI dimers with a lifetime of longer than 5 s (Supplementary Fig. 13c), supporting our finding that unfolded substrates induce formation of long-lived PDI dimers. To exclude the possibility that the PDI dimers were stabilized through binding of the His_6-tag segment to the Co^{2+}-conjugated mica plates, we performed the same HS-AFM analysis using ΔHis-PDI instead of His_6-tagged PDI. Again, significantly more PDI dimers with lifetimes of longer than 5 s were observed in the presence of reduced/denatured RNase A (Supplementary Fig. 13b). This was also the case with reduced/denatured BPTI, although to a lesser extent (Supplementary Fig. 13b). Therefore, it is most likely that PDI dimers were stabilized by the added substrate, not by binding of the His_6-tag segment to the mica plate. Consistent with this, reduced/unfolded BPTI and RNase A increased the proportion of PDI dimers to a different extent (by 15.2% and 28.3%, respectively) (Fig. 6c), indicating that the lifetime of PDI dimers depends on folding status and/or rate of substrates.

Although the central cavity formed by the PDI dimers has significant plasticity as demonstrated earlier, its substrate capacity is likely restricted by the cavity size limit. To determine how PDI deals with much larger substrates than BPTI and RNase A, we employed plasminogen with a molecular weight of approximately 90 kDa and 24 disulfide bonds as a substrate and visualized actions of PDI on unfolded plasminogen by HS-AFM. Cys-blocked plasminogen, in which cysteines were blocked with NEM, showed extended and flexible conformations (Supplementary Fig. 14a). Notably, when we added PDI to Cys-blocked plasminogen, two PDI dimers bound to an unstructured chain of plasminogen during the observation time window of approximately 20 s (Supplementary Fig. 14b and Supplementary Video 5). Such long-lived PDI dimers were observed also with Cys-blocked BPTI (Supplementary Fig. 7b) though located in a more isolated manner (Supplementary Fig. 7d), suggesting the generality of unfolded substrate-induced dimerization of PDI (Fig. 3b).

To further generalize our conclusions regarding multiple PDI dimers acting on larger substrates, we tested another substrate, laminin-511, which contains three intramolecular disulfide bonds in its 87 kDa α5 chain and one intermolecular disulfide bond between its β1 chain (26 kDa) and γ1 chain (28 kDa)[38]. Again, we observed that two PDI dimers bound Cys-blocked laminin-511 in extended and flexible conformations (Supplementary Fig. 14c,d). Thus, large substrates that exceed the capacity of the cavity of a PDI dimer likely recruit multiple PDI dimers to allow oxidative folding simultaneously at multiple sites.

Discussion

Previous studies have demonstrated that PDI dimers can be formed via the **b′** domain without substrates, leading to regulated substrate access to the enzyme[25,27,39,40]. Consistently, our HS-AFM and SEC-MALS analyses revealed that nearly 10% of PDI molecules form dimers even in the absence of substrates (Figs. 3b and 5b). In addition, the present study revealed that unfolded substrates in solution induced strikingly different types of PDI dimers in which the PDI molecules interacted with each other in a face-to-face manner through mutual contacts at one or both ends of each protein (Fig. 3a). Importantly, PDI dimers greatly accelerated disulfide bond introduction into unfolded substrates, rather than inhibiting oxidative folding. Thus, there could be multiple types of PDI dimers with different conformations and physiological functions. Indeed, PDI dimers have been observed in living cells[39], although their physiological significance remains to be determined.

Our HS-AFM analysis also revealed that oxidized PDI is in equilibrium between the open and closed conformations, whereas reduced PDI maintains a closed/twisted conformation. In this context, only the oxidized form could form substrate-induced homodimers with morphological diversity. In the case of large substrates that exceeded the capacity of a PDI dimer, multiple PDI dimers bound different sites of the substrate possibly to promote oxidative folding in a concerted manner. Such heterogeneous conformations of PDI dimers suggest an adaptation to the variable configurations and folding states of substrate proteins. PDI dimers had different lifetimes depending on substrates: the dimers induced by RNase A, whose folding is slower and more complex than that of BPTI[15], persisted longer than the BPTI-induced dimers, undergoing repeated expansion and contraction. Thus, the lifespans of PDI dimers likely correlate with the time required for their substrates to attain folding intermediates or native structures via disulfide bond formation. This conformational adaptability of PDI to substrates likely makes the enzyme more competent as a folding catalyst than other PDIs. Altogether, we propose a mechanism for the operation of PDI engaged in catalysis of oxidative protein folding (for more details, see Fig. 6d).

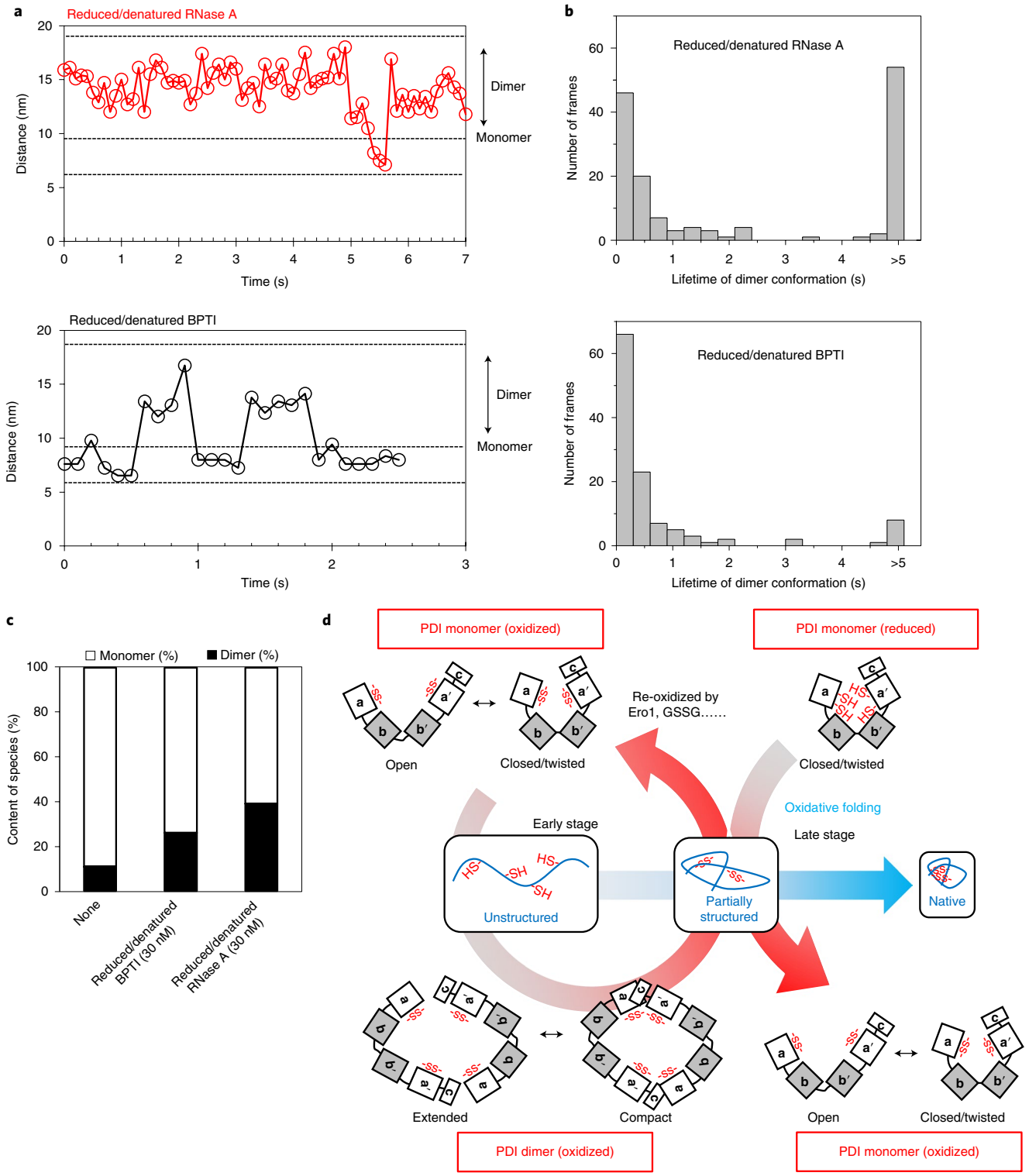

Fig. 6 | PDI dimerization induced by unfolded RNase A. a, Repeated expansion and contraction in the long-axis length of PDI dimers during the catalysis of oxidative folding of RNase A (top) or BPTI (bottom). The experiments were independently repeated 82 times for reduced/denatured RNase A and 61 times for reduced/denatured BPTI, and the same trends were seen in all of the experiments. **b**, Lifetimes of PDI dimers in the presence of reduced/denatured RNase A (top) or BPTI (bottom) ($n = 147$ or 118 independent particles, respectively). **c**, Dimer-to-monomer ratio of oxidized PDI (1 nM) in the absence ($n = 315$ independent particles) or presence of 30 nM reduced/denatured BPTI ($n = 281$ independent particles) or RNase A ($n = 307$ independent particles), as determined by HS-AFM. **d**, Proposed model of the PDI cycle for catalysis of oxidative protein folding. Oxidized PDI captures an unstructured substrate, taking advantage of its conformational dynamics, and forms face-to-face homodimers with weak or transient interactions. The resultant transformable central cavity, which contains multiple redox-active sites and hydrophobic surfaces, accommodates the substrate and efficiently introduces disulfide bonds into it. Partially structured intermediates are then acted on, primarily by monomeric reduced PDI, for proofreading of non-native disulfide bonds. During this process, the less-mobile closed conformation of reduced PDI may guide still-immature intermediates into their proper folding pathways due to its unfoldase activity. Ultimately, correctly folded proteins with native disulfide bonds and hydrophilic surfaces are released from PDI.

An increasing number of studies have reported a link between the disulfide chemistry and the pathogenesis of misfolding diseases. PDI is regarded as a novel target for treatment of several neurodegenerative disorders, including Alzheimer's disease[8,9] and amyotrophic lateral sclerosis[10]. Some PDI mutations, including one at Arg300 (noted in this study), cause striking alterations in motor neuron morphology and impair expression of synaptic proteins, thereby degrading motor performance[10]. Our results suggest that functional defects of PDI mutants can be caused by impairment in redox-dependent conformational switching. Further studies should seek to clarify the dynamic behaviors of this versatile enzyme, thereby helping to elucidate the detailed mechanism of redox-based protein quality control in the ER.

Online content

Any methods, additional references, Nature Research reporting summaries, source data, statements of data availability and associated accession codes are available at https://doi.org/10.1038/s41589-019-0268-8.

Received: 27 April 2018; Accepted: 7 March 2019;
Published online: 15 April 2019

References

1. Hartl, F. U., Bracher, A. & Hayer-Hartl, M. Molecular chaperones in protein folding and proteostasis. *Nature* **475**, 324–332 (2011).
2. Sato, Y. & Inaba, K. Disulfide bond formation network in the three biological kingdoms, bacteria, fungi and mammals. *FEBS J.* **279**, 2262–2271 (2012).
3. Bulleid, N. J. & Ellgaard, L. Multiple ways to make disulfides. *Trends Biochem. Sci.* **36**, 485–492 (2011).
4. Chen, Y. et al. SPD—a web-based secreted protein database. *Nucleic Acids Res.* **33**, D169–D173 (2005).
5. Arolas, J. L., Aviles, F. X., Chang, J. Y. & Ventura, S. Folding of small disulfide-rich proteins: clarifying the puzzle. *Trends Biochem. Sci.* **31**, 292–301 (2006).
6. Okumura, M., Shimamoto, S. & Hidaka, Y. Chemical methods for producing disulfide bonds in peptides and proteins to study folding regulation. *Curr. Protoc. Protein Sci.* **76**, 7.1–7.13 (2014).
7. Weissman, J. S. & Kim, P. S. Reexamination of the folding of BPTI: predominance of native intermediates. *Science* **253**, 1386–1393 (1991).
8. Uehara, T. et al. S-Nitrosylated protein-disulphide isomerase links protein misfolding to neurodegeneration. *Nature* **441**, 513–517 (2006).
9. Hoffstrom, B. G. et al. Inhibitors of protein disulfide isomerase suppress apoptosis induced by misfolded proteins. *Nat. Chem. Biol.* **6**, 900–906 (2010).
10. Woehlbier, U. et al. ALS-linked protein disulfide isomerase variants cause motor dysfunction. *EMBO J.* **35**, 845–865 (2016).
11. Okumura, M., Kadokura, H. & Inaba, K. Structures and functions of protein disulfide isomerase family members involved in proteostasis in the endoplasmic reticulum. *Free Radic. Biol. Med.* **83**, 314–322 (2015).
12. Hatahet, F. & Ruddock, L. W. Protein disulfide isomerase: a critical evaluation of its function in disulfide bond formation. *Antioxid. Redox Signal.* **11**, 2807–2850 (2009).
13. Lyles, M. M. & Gilbert, H. F. Catalysis of the oxidative folding of ribonuclease A by protein disulfide isomerase: dependence of the rate on the composition of the redox buffer. *Biochemistry* **30**, 613–619 (1991).
14. van den Berg, B., Chung, E. W., Robinson, C. V., Mateo, P. L. & Dobson, C. M. The oxidative refolding of hen lysozyme and its catalysis by protein disulfide isomerase. *EMBO J.* **18**, 4794–4803 (1999).
15. Weissman, J. S. & Kim, P. S. Efficient catalysis of disulphide bond rearrangements by protein disulphide isomerase. *Nature* **365**, 185–188 (1993).
16. Kojima, R. et al. Radically different thioredoxin domain arrangement of ERp46, an efficient disulfide bond introducer of the mammalian PDI family. *Structure* **22**, 431–443 (2014).
17. Sato, Y. et al. Synergistic cooperation of PDI family members in peroxiredoxin 4-driven oxidative protein folding. *Sci. Rep.* **3**, 2456 (2013).
18. Inaba, K. et al. Crystal structures of human Ero1α reveal the mechanisms of regulated and targeted oxidation of PDI. *EMBO J.* **29**, 3330–3343 (2010).
19. Kanemura, S. et al. Human ER oxidoreductin-1α (Ero1α) undergoes dual regulation through complementary redox interactions with protein-disulfide isomerase. *J. Biol. Chem.* **291**, 23952–23964 (2016).
20. Masui, S., Vavassori, S., Fagioli, C., Sitia, R. & Inaba, K. Molecular bases of cyclic and specific disulfide interchange between human ERO1α protein and protein-disulfide isomerase (PDI). *J. Biol. Chem.* **286**, 16261–16271 (2011).
21. Wang, L. et al. Reconstitution of human Ero1-Lα/protein-disulfide isomerase oxidative folding pathway in vitro. Position-dependent differences in role between the a and a′ domains of protein-disulfide isomerase. *J. Biol. Chem.* **284**, 199–206 (2009).
22. Edman, J. C., Ellis, L., Blacher, R. W., Roth, R. A. & Rutter, W. J. Sequence of protein disulphide isomerase and implications of its relationship to thioredoxin. *Nature* **317**, 267–270 (1985).
23. Klappa, P., Ruddock, L. W., Darby, N. J. & Freedman, R. B. The b′ domain provides the principal peptide-binding site of protein disulfide isomerase but all domains contribute to binding of misfolded proteins. *EMBO J.* **17**, 927–935 (1998).
24. Tian, G., Xiang, S., Noiva, R., Lennarz, W. J. & Schindelin, H. The crystal structure of yeast protein disulfide isomerase suggests cooperativity between its active sites. *Cell* **124**, 61–73 (2006).
25. Tian, G. et al. The catalytic activity of protein-disulfide isomerase requires a conformationally flexible molecule. *J. Biol. Chem.* **283**, 33630–33640 (2008).
26. Okumura, M. et al. Inhibition of the functional interplay between endoplasmic reticulum (ER) oxidoreductin-1α (Ero1α) and protein-disulfide isomerase (PDI) by the endocrine disruptor bisphenol A. *J. Biol. Chem.* **289**, 27004–27018 (2014).
27. Wang, C. et al. Structural insights into the redox-regulated dynamic conformations of human protein disulfide isomerase. *Antioxid. Redox Signal.* **19**, 36–45 (2013).
28. Serve, O. et al. Redox-dependent domain rearrangement of protein disulfide isomerase coupled with exposure of its substrate-binding hydrophobic surface. *J. Mol. Biol.* **396**, 361–374 (2010).
29. Tsai, B., Rodighiero, C., Lencer, W. I. & Rapoport, T. A. Protein disulfide isomerase acts as a redox-dependent chaperone to unfold cholera toxin. *Cell* **104**, 937–948 (2001).
30. Lumb, R. A. & Bulleid, N. J. Is protein disulfide isomerase a redox-dependent molecular chaperone? *EMBO J.* **21**, 6763–6770 (2002).
31. Cho, K. et al. Redox-regulated peptide transfer from the transporter associated with antigen processing to major histocompatibility complex class I molecules by protein disulfide isomerase. *Antioxid. Redox Signal.* **15**, 621–633 (2011).
32. Kosuri, P. et al. Protein folding drives disulfide formation. *Cell* **151**, 794–806 (2012).
33. Kodera, N., Yamamoto, D., Ishikawa, R. & Ando, T. Video imaging of walking myosin V by high-speed atomic force microscopy. *Nature* **468**, 72–76 (2010).
34. Uchihashi, T., Iino, R., Ando, T. & Noji, H. High-speed atomic force microscopy reveals rotary catalysis of rotorless F_1-ATPase. *Science* **333**, 755–758 (2011).
35. Uchihashi, T., Kodera, N. & Ando, T. Guide to video recording of structure dynamics and dynamic processes of proteins by high-speed atomic force microscopy. *Nat. Protoc.* **7**, 1193–1206 (2012).
36. Noi, K. et al. High-speed atomic force microscopic observation of ATP-dependent rotation of the AAA + chaperone p97. *Structure* **21**, 1992–2002 (2013).
37. Irvine, A. G. et al. Protein disulfide-isomerase interacts with a substrate protein at all stages along its folding pathway. *PLoS ONE* **9**, e82511 (2014).
38. Ido, H. et al. The requirement of the glutamic acid residue at the third position from the carboxyl termini of the laminin gamma chains in integrin binding by laminins. *J. Biol. Chem.* **282**, 11144–11154 (2007).
39. Bastos-Aristizabal, S., Kozlov, G. & Gehring, K. Structural insight into the dimerization of human protein disulfide isomerase. *Protein Sci.* **23**, 618–626 (2014).
40. Wallis, A. K. et al. The ligand-binding b′ domain of human protein disulphide-isomerase mediates homodimerization. *Protein Sci.* **18**, 2569–2577 (2009).

Acknowledgements

Synchrotron radiation experiments were performed on BL45XU in SPring-8 with the approval of RIKEN (proposal no. 2014A1345). We are grateful to M. Matsusaki, S. Kanbayashi and S. Ogawa for their experimental assistance. This work was supported by funding from CREST (to T.O. (JPMJCR13M1) and K.I. (JPMJCR13M6)), Grant-in-Aids for Scientific Research on Innovative Areas from MEXT (to K.I. (26116005) and M.O. (15641922)), the Takeda Science Foundation (to K.I. and M.O.), the Uehara Memorial Foundation (to K.I. and M.O.), the Naito Foundation (to M.O.), a Grant-in-Aid for JSPS Fellows (to M.O. and K.S.), the Building of Consortia for the Development of Human Resources in Science and Technology (to M.O.), the program of the Joint Usage/Research Center for Developmental Medicine (IMEG, Kumamoto University) (to M.O. and K.I.), and the Nanotechnology Platform Program (Molecule and Material Synthesis) of MEXT (to M.O., S.K., S.A. and K.I.).

Author contributions

M.O. designed and performed almost all experiments including the SAXS, HS-AFM and oxidative protein folding experiments. K.N. performed AFM measurements, and

analyzed the HS-AFM data. S.K. performed SAXS experiments. M.K. performed ITC experiments and statistical analysis using AIC scores. T.S. performed SEC-MALS experiments. Y.I. analyzed the AFM images. T.H. assisted the SAXS experiment. S.A. analyzed the SAXS data. T.O. assisted with HS-AFM experiments and reviewed the manuscript. K.I. supervised the study. K.I. and M.O. wrote the manuscript. M.O. prepared figures. All authors discussed the results and approved the manuscript.

Competing interests

The authors declare no competing interests.

Additional information

Supplementary information is available for this paper at https://doi.org/10.1038/s41589-019-0268-8.

Correspondence and requests for materials should be addressed to M.O., T.O. or K.I.

Methods

Sample preparation. Human PDI used in this study was overexpressed and purified as described previously[16,17]. To prepare PDI without the His_6-tag, the tag segment was cleaved off by digestion with thrombin (Nacalai Tesque; 0.2 U mg^{-1}) at 4 °C for 24 h. The digested sample was separated by SEC using a Superdex 200 10/300 Increase column (GE Healthcare). For preparation of reduced or oxidized PDI, purified PDI was incubated in buffer A (50 mM Tris-HCl, pH 7.5 and 300 mM NaCl) containing 1 mM DTT (reduced form) or 1 mM diamide (oxidized form) on ice for 10 min. After incubation, DTT or diamide was removed by gel filtration on a Superdex 200 10/300 Increase column. Redox states of PDI prepared in this manner were confirmed by SDS–PAGE after modification with a thiol-alkylating agent, maleimide-PEG-2k.

High-speed AFM imaging. Single-molecule images of PDI were observed on a high-speed AFM built in Toshio Ando's group (Kanazawa University)[33–36,41]. The His_6-tag at the N-terminus of PDI was immobilized on a Co^{2+}-scattered mica surface. After treatment of the mica surface with cobalt chloride (100 mM) for 3 min, the surface was washed with buffer A. For immobilization, a droplet (10 µl) containing 1 nM PDI was loaded onto the mica surface. After 3 min of incubation, the surface was washed with buffer A. All solutions were degassed with N_2 gas, and the reactions were carried out in a sealed vial under an N_2 atmosphere. Single-molecule imaging was performed in tapping mode (spring constant, ~0.1 N m^{-1}; resonant frequency, 0.8–1 MHz; quality factor in water, ~2) and analyzed using software developed by Toshio Ando's group (Kanazawa University), Kodec4.4.7.39[33–36,41]. AFM observations were made in fixed imaging areas (400 × 400 $Å^2$) at a scan rate of 0.1 s $frame^{-1}$. Each molecule was observed separately on a single frame with the highest pixels (60 × 60 pixels). Cantilevers (Olympus) were 6–7 µm long, 2 µm wide and 90 nm thick. The microscope probe tips were grown on a cantilever by electron beam deposition and further sharpened by argon plasma etching[42]. For AFM imaging, the free oscillation amplitude was set to approximately 1 nm, and the set-point amplitude was around 80% of the free oscillation amplitude. The estimated tapping force was less than 30 pN (ref. [43]). A low-pass filter was used to remove noise from acquired images. The area of a single PDI molecule in each frame was calculated using LabView 2013 (National Instruments) with custom-made programs. The circular area of PDI, which was determined using a constant threshold of 110, was fitted with an ellipsoid to obtain the dimensions of the half-major axis (a) and half-minor axis (b). Then, the area of the ellipsoid (πab) was calculated and taken as the area of PDI. To probe the dynamic behavior of assembly and disassembly of PDI, the largest area in each frame was plotted as a function of time (Fig. 3f).

SAXS experiments. SAXS data were collected at the SPring-8 BL45XU RIKEN beamline (Hyogo, Japan). The X-ray wavelength was 1.0 Å, and detection was performed on a PILATUS 300K-W at a camera distance of 1,999.890 mm. The X-ray scattering intensities were recorded at 293.2 K as a continuous series of scattering images taken with an exposure time of 1.0 s for both oxidized and reduced PDI[16,26]. Reduced PDI for the SAXS measurement was prepared in buffer B (10 mM phosphate, pH 8.0 and 150 mM NaCl, 5% glycerol) containing 1 mM DTT as a reducing reagent. For preparation of oxidized PDI, purified PDI was incubated on ice for 10 min in buffer B containing 5 mM $K_3[Fe(CN)_6]$ as an oxidizing reagent. After incubation, $K_3[Fe(CN)_6]$ was removed by SEC using a Superdex 200 10/300 Increase column (GE Healthcare). Redox states of PDI were confirmed by SDS–PAGE in combination with the thiol-alkylating agent, maleimide-PEG-2k. SAXS data of PDI were collected in the concentration range 0.87–5.24 mg ml^{-1} for the oxidized form and 0.96–5.91 mg ml^{-1} for the reduced form. SAXS data for bovine serum albumin (Sigma-Aldrich) were also collected for use as a standard for molecular mass determination of PDI[44]. These data treatments resulted in scattering patterns, $I(Q)$, where $Q = 4\pi\sin\theta/\lambda$, 2θ is the scattering angle, and λ is the wavelength of the X-ray. SAXS profiles were fitted under the Guinier approximation according to equation (1):

$$I(Q) = I(0)\exp(-Rg^2Q^2/3) \quad (1)$$

where $I(0)$ and R_g are the forward scattering intensity at $Q=0$ and the radius of gyration, respectively. The $I(0)$ value normalized relative to the concentration (mg ml^{-1}) is proportional to the molecular mass. The pair distribution function, $P(r)$, was calculated from indirect Fourier transformation using the GNOM package[45]. The theoretical SAXS curves were calculated from crystal structures (Protein Data Bank codes: 4EL1 for oxidized and 4EKZ for reduced PDI) using the CRYSOL package[46].

BPTI modification. For preparation of Cys-blocked BPTI, the lyophilized reduced and denatured BPTI (40 nmol) was dissolved in 10 µl of 0.05% trifluoroacetic acid (TFA) and 2 M urea, and then modified with maleimide by addition of 190 µl of 0.1 M Tris-HCl pH 7.0, 1% SDS and 1 mg ml maleimide-ATTO532 (ATTO-TEC) for 3 h at 30 °C (ref. [6]). All solutions were degassed by flushing N_2 gas, and the reactions were carried out in a sealed vial under an N_2 atmosphere. The resultant sample was purified by RP-HPLC using an InertSustain C18 HPLC column (4.6 × 150 mm; GL Sciences) at a flow rate of 1.0 ml min^{-1}. Cys-blocked BPTI was eluted by a linear gradient of 95% buffer C (0.05% TFA in water) and 5% buffer D (0.05% TFA in acetonitrile) at 0 min to 60% buffer C and 40% buffer D at 55 min. Separated fractions were lyophilized and then subjected to MALDI-TOF/MS analysis for their confirmation (Supplementary Fig. 7a). For purification of N* BPTI, reduced and denatured BPTI (50 µM) was dissolved in buffer A containing 2 mM GSH and 1 mM GSSG. The reaction was quenched with an equivalent volume of 1 M HCl after incubation for 1 h, and N* BPTI was separated by RP-HPLC on a TSKgel Protein C_4-300 column (4.6 × 150 mm; Tosoh Bioscience) (Supplementary Fig. 11). N* BPTI was eluted by two-step linear gradients of 95% buffer C and 5% buffer D at 0 min to 80% buffer C and 20% buffer D at 15 min, and then to 30% buffer C and 70% buffer D at 115 min. For preparation of NEM-modified N* BPTI, purified N* BPTI (100 nmol) was incubated with 5 mM NEM at 30 °C at pH 7.5 for 3 h, separated by RP-HPLC using a TSKgel Protein C4-300 column (4.6 × 150 mm; Tosoh Bioscience) with monitoring by UV absorption at 229 nm, and confirmed by MALDI-TOF/MS (Supplementary Fig. 9b,c). NEM-modified N* BPTI was eluted by a linear gradient of 95% buffer C and 5% buffer D at 0 min to 60% buffer C and 40% buffer D at 50 min. For preparation of Au-conjugated BPTI, reduced/denatured BPTI (40 nmol) was dissolved in 10 µl of 0.05% TFA and 6 M urea, and diluted with 190 µl of 0.1 M Tris-HCl pH 8.0 containing Au colloid with a diameter of 2 nm (BBI Solutions). The reaction mixture was incubated at 30 °C for 3 h [6], and the resulting sample was separated by HPLC to remove free Au colloid. Au-conjugated BPTI was eluted by a linear gradient of 95% buffer C and 5% buffer D at 0 min to 60% buffer C and 40% buffer D at 55 min. Au-conjugated BPTI was confirmed by MALDI-TOF/MS analysis. The concentrations of modified BPTIs were determined by the BCA method[26].

MALDI-TOF/MS analysis. Purified and lyophilized samples (~0.1 nmol) were dissolved in 0.5 µl of 0.05% TFA/50% acetonitrile, and dissolved samples were mixed with 0.5 µl of a matrix solution (10 mg ml^{-1}) and air dried on the target plate (Bruker Japan) for MALDI-TOF/MS. Molecular masses were determined on a Daltonics autoflex spectrometer (Bruker Japan) in positive-ion mode. Mass spectrometric analyses were performed in the linear mode using 3,5-dimethoxy-4-hydroxycinnamic acid (Tokyo Chemical Industry) as a matrix. The molecular mass was calculated using the Protein-Prospector web server (http://prospector.ucsf.edu/prospector/mshome.htm).

NADPH consumption assay. NADPH consumption coupled to PDI or PDI R300A oxidation by Ero1α was measured by monitoring the decrease in absorbance at 340 nm on a HITACHI U-3310 spectrophotometer at 30 °C (refs. [17,26]). The reaction mixture contained 200 µM NADPH, 1 U glutathione reductase, 1 mM GSH, 2 µM Ero1α and 10 µM PDI/PDI R300A in buffer A. The buffer A was saturated with oxygen before experiments.

RNase A refolding assay. RNase A from bovine pancreas (Sigma-Aldrich) was dissolved in buffer A containing 6 M guanidinium hydrochloride and 200 mM DTT and incubated for 5 h at 30 °C (ref. [17]). The resulting sample was loaded onto a PD-10 column to remove the denaturing and reducing reagents. Reduced and denatured RNase A (25 µM) was incubated for 0–30 min at 30 °C with 1 µM PDI/PDI R300A and 2 µM Ero1α in a buffer A. The buffer was saturated with oxygen before experiments. After addition of 4 mM cytidine 2′,3′-cyclic monophosphate monosodium salt (Sigma-Aldrich) to aliquots, RNase A activity was monitored the linear increase in absorbance at 295 nm on a Hitachi U-3310 spectrophotometer at 30 °C. Values represent means ± s.d. from three independent experiments.

BPTI refolding assay. Reduced and denatured BPTI (50 µM) was dissolved in buffer A containing 2 mM GSH, 1 mM GSSG and PDI, as described previously[16,26]. All solutions used in this experiment were degassed by flushing N_2 gas, and folding reactions were carried out in a sealed vial under an N_2 atmosphere at 30 °C. The reaction mixtures (200 µl aliquots) were quenched with an equivalent volume of 1 M HCl at the selected time points and folding intermediates were separated by RP-HPLC on a TSKgel Protein C_4-300 column (4.6 × 150 mm; Tosoh Bioscience) with monitoring at 229 nm. Folding intermediates of BPTI were separated by a two-step linear gradient of 95% buffer C and 5% buffer D at 0 min to 80% buffer C and 20% buffer D at 15 min, and then to 30% buffer C and 70% buffer D at 115 min. The folding intermediates thus obtained were identified by MALDI-TOF/MS analysis as described above. Values represent the means ± s.d. from five independent experiments. The kinetic rate constants for folding reactions were determined by curve fitting with the statistical software IGOR Pro 6.0 (WaveMetrics).

Plasminogen and laminin-511 modification. Plasminogen (1.0 mg ml^{-1}) (Wako Pure Chemical Industries) was dissolved in buffer A containing 8 M urea and 20 mM DTT and the solution was allowed to stand for 5 h at 50 °C. The reaction mixture was loaded onto a PD-10 column to remove the denaturing and reducing reagents. Redox states of reduced plasminogen were confirmed by SDS–PAGE after modification with thiol-alkylating agent, NEM. For NEM-modification, reduced plasminogen (25 µM) was incubated at 37 °C in buffer A containing NEM (5 mM). Laminin-511 (iMatrix-511) was purchased from Wako Pure Chemical Industries. Laminin-511 (0.5 mg ml^{-1}) was dissolved in buffer A containing 8 M urea and

20 mM DTT and incubated for 4 h at 50 °C. The resulting sample was loaded onto a PD-10 column to remove the denaturing and reducing reagents. Redox states of laminin-511 prepared in this manner were confirmed by SDS–PAGE after modification with thiol-alkylating agent, NEM. For NEM-modification, reduced laminin-511 (~1.5 μM) was incubated at 37 °C in buffer A containing NEM (1 mM). The concentrations of modified plasminogen and laminin-511 were determined by the BCA method.

Isothermal titration calorimetry measurements. Isothermal titration calorimetry (ITC) was carried out on a MicroCal ITC200 calorimeter (Malvern Panalytical) at 298 K and 500 r.p.m. All measurements were performed in buffer containing 50 mM Tris-HCl buffer (pH 7.5) and 150 mM NaCl. All proteins were centrifuged at 10,000 r.p.m. for 2 min at 298 K before use. For experiments, 1.7 μl of the mastoparan solution (1.35 mM) was injected into PDI solution (53.7 μM and 39.6 μM for wild type and R300A, respectively) at 300 s intervals after a 300 s initial delay. To minimize the effect of bubbles and imperfect solution filling of the syringe, the first titration was performed using 0.4 μl of solution in the syringe. Changes in heat flow were observed in real time with 10 μcal s^{-1} of reference power. The data were analyzed using the Microcal Origin software. Data were best fitted by a one-site binding model, and both stoichiometry and affinity values were calculated from the thermograms as previously reported[47].

SEC-MALS experiments. SEC-MALS was performed using a DAWN HELEOS8+ (Wyatt Technology) equipped with a Tosoh liquid chromatography on a TSKgel G3000SWXL (Tosoh) gel-filtration column at a flow rate of 1.0 ml min^{-1}. Protein concentrations were calculated based on differential refractive index (Shimadzu) downstream of MALS. Oxidized PDI was incubated at room temperature with NEM-blocked BPTI in buffer A. After incubation for 20 min, mixtures were centrifuged at 15,000 r.p.m. for 10 min before use. One hundred microliters of supernatant was injected into this system. The data were analyzed using ASTRA version 7.0.1 (Wyatt Technology) as previously described[48].

Model selection of statistical data by AIC. The validity of model selections for a given set of data was evaluated on the basis of the AIC scores[49]. Total area of each histogram was normalized to unity. The model of a single-Gaussian distribution can be expressed as follows:

$$g_i(x) = \frac{1}{\sqrt{2\pi\sigma_i^2}}\exp\left(-\frac{-(x-\mu_i)}{2\sigma_i^2}\right) \quad (2)$$

where μ_i and σ_i indicate the mean and standard deviation of distribution, respectively, and i indicates the index for the following summation. Thus, one- to five-state models can be expressed as follows:

$$f_n(x) = \sum_i^n a_i \times g_i(x) = \sum_i^n \frac{a_i}{\sqrt{2\pi\sigma_i^2}}\exp\left(-\frac{-(x-\mu_i)}{2\sigma_i^2}\right) \quad (3)$$

in which n is the number of the states ($n = 1, 2, 3, 4,$ and 5) and a_i is a scaling factor to adjust the integration of equation (3) to unity according to equation (4):

$$\sum_i^n a_i = 1 \ (0 < a_i < 1) \quad (4)$$

Note that equation (3) contains $3n$ parameters from a_i, μ_i and σ_i. These parameters are optimized by the maximum likelihood estimation; on a logarithmic scale, maximized likelihood is expressed according to the following equation:

$$\ln(L_{n,\max}) = \ln\left(\prod_j f_{n,\max}(x_j)\right) = \sum_j \ln(f_{n,\max}(x_j)) \quad (5)$$

where $L_{\max}$ and x_j indicate the maximized likelihood value and each observed value, respectively, and j means the index for product/summation. Using $\ln(L_{\max})$ and n, the AIC value for a given model is expressed as follows:

$$\mathrm{AIC}_n = -2\ln(L_{n,\max}) + 2(3n-1) \quad (6)$$

The model that yields the lowest AIC value can be regarded as most appropriate[49].

In analysis of two-dimensional distributions, the equations of a bivariate normal distribution can be expressed as follows:

$$G_i(x,y) = \frac{1}{2\pi\sigma_{Xi}\sigma_{Yi}\sqrt{1-\rho_i^2}}\exp\left[-\frac{1}{2(1-\rho_i^2)}\left\{\frac{(x-\mu_{Xi})^2}{\sigma_{Xi}^2} - \frac{2\rho_i(x-\mu_{Xi})(y-\mu_{Yi})}{\sigma_{Xi}\sigma_{Yi}} + \frac{(y-\mu_{Yi})^2}{\sigma_{Yi}^2}\right\}\right] \quad (7)$$

where μ_{Xi} and μ_{Yi} represent the means of the distribution, σ_{Xi} and σ_{Yi} indicate the deviations, and ρ is the correlation between X and Y. Subscripts X and Y mean the corresponding axial directions. Therefore, the model of N distributions can be described as:

$$F_N(x,y) = \sum_i^N a_i \times G_i(x,y) \quad (8)$$

in which N is the number of the states ($N = 1, 2, 3,$ and 4) and a_i is a scaling factor (see equation (4)). Parameters included in equation (8) are optimized by the maximum likelihood method. AIC values for models (F_N) are calculated using maximum likelihood values in logarithmic scale (see equation (5)) and number of parameters as follows:

$$\mathrm{AIC}_N = -2\ln(L_{N,\max}) + 2(6N-1) \quad (9)$$

The model with the lowest AIC value can be regarded as most appropriate.

Statistics and reproducibility. Information on the number of independently observed particles and the number of replicates, along with the statistical test and statistical significance, is provided in the figure legends.

Reporting Summary. Further information on research design is available in the Nature Research Reporting Summary linked to this article.

Data availability

None of the data in this paper have been deposited in public databases. All data in this study are available upon reasonable request.

References

41. Maegawa, K. I. et al. The highly dynamic nature of ERdj5 is key to efficient elimination of aberrant protein oligomers through ER-associated degradation. *Structure* **25**, 846–857.e4 (2017).
42. Wendel, M., Lorenz, H. & Kotthaus, J. P. Sharpened electron beam deposited tips for high resolution atomic force microscope lithography and imaging. *Appl. Phys. Lett.* **67**, 3732–3734 (1995).
43. Rodríguez, T. R. & García, R. Theory of *Q* control in atomic force microscopy. *Appl. Phys. Lett.* **82**, 4821–4823 (2003).
44. Akiyama, S. Quality control of protein standards for molecular mass determinations by small-angle X-ray scattering. *J. Appl. Crystallogr.* **43**, 237–243 (2010).
45. Svergun, D. Mathematical methods in small-angle scattering data analysis. *J. Appl. Crystallogr.* **24**, 485–492 (1991).
46. Svergun, D., Barberato, C. & Koch, M. H. J. CRYSOL—a program to evaluate X-ray solution scattering of biological macromolecules from atomic coordinates. *J. Appl. Crystallogr.* **28**, 768–773 (1995).
47. Kinoshita, M. et al. Physicochemical nature of interfaces controlling ferredoxin NADP$^+$ reductase activity through its interprotein interactions with ferredoxin. *Biochim. Biophys. Acta* **1847**, 1200–1211 (2015).
48. Saio, T., Guan, X., Rossi, P., Economou, A. & Kalodimos, C. G. Structural basis for protein antiaggregation activity of the trigger factor chaperone. *Science* **344**, 1250494 (2014).
49. Akaike, H. A new look at the statistical model identification. *IEEE Trans. Automat. Contr.* **19**, 716–723 (1974).

nature research

Corresponding author(s): Masaki Okumura, Teru Ogura, and Kenji Inaba

Last updated by author(s): Feb 13, 2019

Reporting Summary

Nature Research wishes to improve the reproducibility of the work that we publish. This form provides structure for consistency and transparency in reporting. For further information on Nature Research policies, see Authors & Referees and the Editorial Policy Checklist.

Statistics

For all statistical analyses, confirm that the following items are present in the figure legend, table legend, main text, or Methods section.

n/a	Confirmed	
☐	☒	The exact sample size (*n*) for each experimental group/condition, given as a discrete number and unit of measurement
☐	☒	A statement on whether measurements were taken from distinct samples or whether the same sample was measured repeatedly
☒	☐	The statistical test(s) used AND whether they are one- or two-sided *Only common tests should be described solely by name; describe more complex techniques in the Methods section.*
☒	☐	A description of all covariates tested
☒	☐	A description of any assumptions or corrections, such as tests of normality and adjustment for multiple comparisons
☐	☒	A full description of the statistical parameters including central tendency (e.g. means) or other basic estimates (e.g. regression coefficient) AND variation (e.g. standard deviation) or associated estimates of uncertainty (e.g. confidence intervals)
☒	☐	For null hypothesis testing, the test statistic (e.g. *F*, *t*, *r*) with confidence intervals, effect sizes, degrees of freedom and *P* value noted *Give P values as exact values whenever suitable.*
☒	☐	For Bayesian analysis, information on the choice of priors and Markov chain Monte Carlo settings
☒	☐	For hierarchical and complex designs, identification of the appropriate level for tests and full reporting of outcomes
☒	☐	Estimates of effect sizes (e.g. Cohen's *d*, Pearson's *r*), indicating how they were calculated

Our web collection on statistics for biologists contains articles on many of the points above.

Software and code

Policy information about availability of computer code

Data collection	High-speed AFM imaging data were collected using Kodec4.4.7.39, a software originally developed in Dr Toshio Ando's group at Kanazawa University. SAXS data were collected using DetectorControl, a software originally developed in SPring8 BL45XU.
Data analysis	For analysis of high-speed AFM images, the area of a single PDI molecule in each frame was calculated using LabView 2013 (National Instruments, Austin, USA). The average length of each dimension (means ± SD) was calculated using the Origin 6.0 software. For analysis of SAXS data, the pair distribution function, P(r), was calculated from indirect Fourier transformation using the GNOM 4.6, and the theoretical SAXS curves of crystal structures were calculated using CRYSOL 2.8.3. For analysis of folding kinetics data, the rate constants were determined using the statistical software IGOR Pro6 (WaveMetrics, Inc.). For analysis of SEC-MALS, the data were analyzed using ASTRA version 7.0.1 (Wyatt Technology Corporation, Santa Barbara California, USA). For analysis of ITC, the data were analyzed using the Microcal Origin software version 7.0552.

For manuscripts utilizing custom algorithms or software that are central to the research but not yet described in published literature, software must be made available to editors/reviewers. We strongly encourage code deposition in a community repository (e.g. GitHub). See the Nature Research guidelines for submitting code & software for further information.

Data

Policy information about availability of data

All manuscripts must include a data availability statement. This statement should provide the following information, where applicable:

- Accession codes, unique identifiers, or web links for publicly available datasets
- A list of figures that have associated raw data
- A description of any restrictions on data availability

All data generated or analyzed during this study are included in this article and its supplementary information files.

Field-specific reporting

Please select the one below that is the best fit for your research. If you are not sure, read the appropriate sections before making your selection.

☒ Life sciences ☐ Behavioural & social sciences ☐ Ecological, evolutionary & environmental sciences

For a reference copy of the document with all sections, see nature.com/documents/nr-reporting-summary-flat.pdf

Life sciences study design

All studies must disclose on these points even when the disclosure is negative.

Sample size	For statistical analysis of HS-AFM data, more than 100 molecules were counted to draw a confirmative conclusion, as previous studies did so. For statistical analysis, each experiment was performed at least three times to draw a confirmative conclusion, as previous studies did so.
Data exclusions	No data were excluded from the analyses.
Replication	We repeatedly performed independent experiments to ensure that our experimental data could be reliably reproduced.
Randomization	We have chosen observation particles randomly for all statistical analyses. We have not allocated any samples into experimental groups.
Blinding	Blinding was not relevant to this work since we have not done group allocation in any experiments.

Reporting for specific materials, systems and methods

We require information from authors about some types of materials, experimental systems and methods used in many studies. Here, indicate whether each material, system or method listed is relevant to your study. If you are not sure if a list item applies to your research, read the appropriate section before selecting a response.

Materials & experimental systems

n/a	Involved in the study
☒	☐ Antibodies
☒	☐ Eukaryotic cell lines
☒	☐ Palaeontology
☒	☐ Animals and other organisms
☒	☐ Human research participants
☒	☐ Clinical data

Methods

n/a	Involved in the study
☒	☐ ChIP-seq
☒	☐ Flow cytometry
☒	☐ MRI-based neuroimaging